ELSEVIER

### Contents lists available at ScienceDirect

# Aerospace Science and Technology

journal homepage: www.elsevier.com/locate/aescte



# Numerical investigation on high-speed jet actuation for transient control of flow separation



Taesoon Kim<sup>a</sup>, Solkeun Jee<sup>b</sup>, Myungil Kim<sup>a</sup>, Ilyoup Sohn<sup>a,\*</sup>

- a Intelligent Simulation Center, Korea Institute of Science and Technology Information, 245 Daehak-ro, Yuseong-gu, Daejeon, South Korea
- b School of Mechanical Engineering, Gwangju Institute of Science and Technology, 123 Cheomdan-gwagi-ro, Buk-gu, Gwangju 61005, South Korea

# ARTICLE INFO

# Article history: Received 31 August 2022 Accepted 2 February 2023 Available online 13 February 2023 Communicated by Muguru Chandrasekhara

Keywords:
Flow separation
Active flow control
Transient control
Impulsive actuation
Combustion-powered actuation (COMPACT)

### ABSTRACT

Flow separation around a lifting body was controlled using a high-speed jet generated via impulsive actuation, and important flow features associated with the transient dynamics were numerically investigated. A jet flow was impulsively applied to the VR-12 airfoil using a boundary condition modeled as a COMPACT module in the wind tunnel experiments. A delayed detached-eddy simulation based on the Spalart-Allmaras turbulence model was conducted. Computational results indicated that the aerodynamic characteristics quickly varied in the early stage after jet initiation, and that the impact of the actuation on the flow behavior was gradually reduced through a larger time scale than the freestream convection. A detailed investigation was performed to assess relevant flow features, and two distinct flow characteristics associated with the transient dynamics were identified: reattachment and recirculation. Reattachment in the early stage after actuation yielded a high suction peak near the leading edge and rapidly enhanced the lift force. Recirculation in the later stage affected gradual variations in the aerodynamic forces and moment to the baseline flow via the generation of a low-pressure region on the suction side.

© 2023 Elsevier Masson SAS. All rights reserved.

# 1. Introduction

Flow separation can occur at high incidence angles and decrease the aerodynamic performance of a lifting body. Considerable research efforts on flow control have been dedicated to mitigating such critical phenomena to improve aerodynamic performance [1-3]. For example, Gad-el-Hak [1] and Ashill et al. [2] reviewed passive and active control techniques used to produce desired effects such as separation prevention, lift augmentation, and drag reduction. Cattafesta and Sheplak [3] reported on various actuators, covering key features and challenges associated with flow control techniques. It has been shown that passive control methods (e.g., vortex generators, riblets, and grooves) are easy to implement and do not require external energy sources, but can incur unexpected drag in high-speed conditions, which is undesirable. On the other hand, active flow control methods, such as moving surfaces [4-8], plasma [9], and fluidic actuation [10-16], have been utilized in various flow conditions with minimum geometric variation.

Among these various methods, the generation of a highmomentum jet via impulsive actuation was examined in this study. A significant pressure rise due to a chemical process involving a fuel/air mixture in a combustion chamber chokes the flow in the nozzle and generates a high-speed jet of  $Ma \geq 1$  within a short duration of  $\mathcal{O}(10^{-3} \text{ s})$ . This pulsed-blowing-type device is often referred to as a combustion-powered actuator (COMPACT) [17,18], and relevant flow-control studies involving COMPACT actuation are summarized in Table 1.

Crittenden et al. [17] demonstrated that COMPACT actuation can generate a high-momentum jet toward the external flow. The actuator had a size of approximately  $\mathcal{O}(1\text{ ml})$  and was able to handle an operating frequency of  $\mathcal{O}(10^2\text{ Hz})$  using a hydrogen/air mixture. Brzozowski et al. [19] and Woo and Glezer [20] tested the use of actuations to control flows around the NACA 4415 airfoil in wind tunnel experiments and observed rapid changes in circulation from impulsive jet flows. Woo et al. [21] applied COMPACT modules to a rotor–body–interaction (ROBIN) mod7 fuselage and showed reductions in the total drag with repetitively pulsed actuations along the flat surface of the ramp. Matalanis et al. [22–24] and Tan et al. [25] installed COMPACT actuators near the leading edge of the VR-12 airfoil to suppress dynamic stall events in rotor-relevant flow con-

<sup>\*</sup> Corresponding author.

E-mail address: sohniy@kisti.re.kr (I. Sohn).

**Table 1**Selected flow-control studies with COMPACT actuation

Investigator(s)	Method	Re (×10 <sup>6</sup> )	Ма	Lifting Body
Crittenden et al. [17]	EXP	-	-	-
Brzozowski et al. [19]	EXP	0.57	-	NACA 4415
Woo and Glezer [20]	EXP	0.57	-	NACA 4415
Woo et al. [21]	EXP	1.1	-	ROBIN mod7
Matalanis et al. [22-24]	EXP	1.7-3.5	0.2-0.4	VR-12
Tan et al. [25]	EXP	0.54-1.07	0.06-0.12	VR-12
Jee et al. [26]	URANS	1.7-3.5	0.2-0.4	VR-12
Kim et al. [27-29]	URANS	2.6	0.3	VR-12

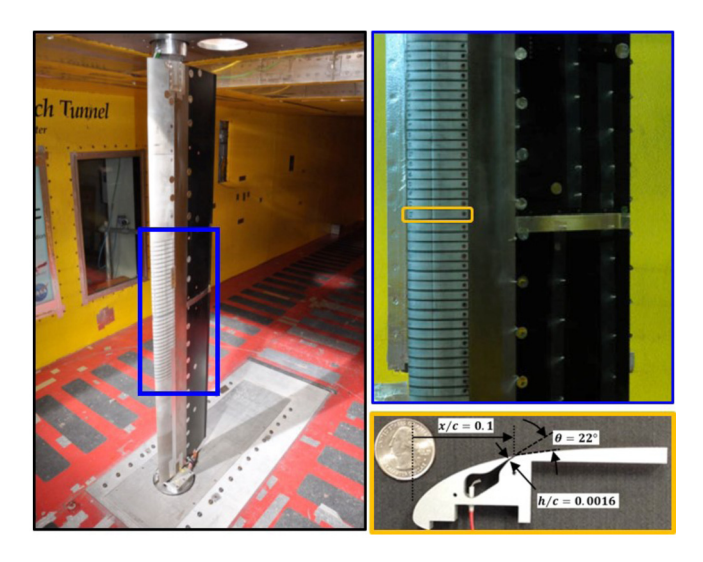


Fig. 1. VR-12 wing with COMPACT installed in Glenn icing research tunnel [23,24].

ditions (see Fig. 1). Computational studies on using the unsteady Reynolds-averaged Navier–Stokes (URANS) approach [26–29] have also been reported, which applied the COMPACT actuation to control dynamic stall. A temporally accurate actuator boundary condition has been proposed to model impulsive actuation, and jet flows were successively applied to the computational domain based on measurements from wind tunnel tests [23,24]. Numerical investigations revealed that compressible flow computation may be imperative mainly because of the choked flow at the nozzle throat, which drives high-speed jets into the external flow.

Although impulsive actuation has demonstrated in wind tunnel tests its significant impact on controlling external flows, experimental studies have focused mainly on variations in the aerodynamic forces and moment with respect to the actuation. Furthermore, the URANS approach could be adopted to test multiple actuation parameters, it incorporates an unexpected numerical dissipation, which could limit the capture of detailed turbulent structures. Therefore, the primary objective of the current study is to numerically investigate a detailed flow-control mechanism of impulsive actuation for the transient control of separated flow, which can complement previous experimental studies. Specifically, a recent wind tunnel test on a VR-12 wing under high-speed flow conditions [24] was numerically solved in this study via an eddyresolving simulation based on a delayed detached-eddy simulation (DDES) turbulence model.

The remainder of this work is organized as follows. The computational methods, including the numerical schemes and actuator models, are presented in Sections 2.1 and 2.2. The baseline flow is described in Section 3.1, and detailed investigations on the transient dynamics with impulsive actuation are discussed in Section 3.2. Finally, the conclusions of this study are presented in Section 4.



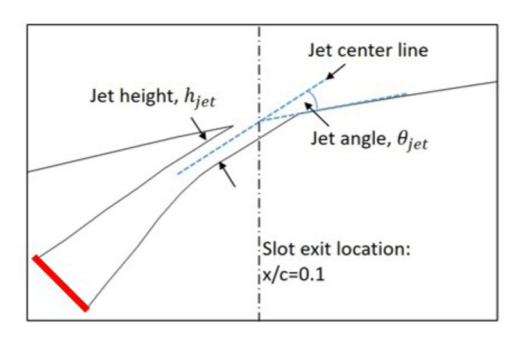


Fig. 2. VR-12 airfoil with an actuator slot.

# 2. Computational methodology

# 2.1. Numerical setups

A VR-12 airfoil with a 0.05c trailing-edge tab tested in the NASA Glenn Icing Research Tunnel [22–24] was simulated (see Fig. 2). The actuator slot was located at x/c=0.1 (based on the slot exit) with a jet height of  $h_{jet}/c=0.0016$ . The jet angle was  $\theta_{jet}=22^{\circ}$  because previous relevant studies [22,28] have suggested that tangential blowing outperforms normal blowing because of additional jet momentum to the boundary layer. The flow conditions of the current simulation were Ma=0.3 and  $Re=2.6\times10^6$  based on the freestream velocity  $U_{\infty}$ , air density  $\rho_{\infty}$ , and viscosity  $\mu_{\infty}$ . An angle of attack of  $\alpha=20^{\circ}$ , which has resulted in massively separated flows around the lifting surface [23,24,26–31], was considered. The moment center was located at (x,z)=(0.25c,0.0223c).

The computational grids tested in the baseline simulation are summarized in Table 2. The O-type grid was generated in the streamwise  $\xi$  and wall-normal  $\zeta$  directions, mainly because of the rounded trailing edge (see Fig. 3). The freestream boundary was located 40c away from the airfoil. Three-dimensional grids were generated via the extrusion of the O-type grid to the span direction  $\eta$  to allocate isotropic cells in the focus region for eddy resolving simulation. The overall strategy for the grid generation was based on the guidelines by Spalart and Streett [32].

The conservative forms of the compressible Navier-Stokes equations were numerically solved using the flow solver CFL3D [33]. Roe's flux-differencing scheme [34] with a third-order monotonic upstream-centered scheme for conservation laws (MUSCL) was used for the convective fluxes, and central differencing was used for the viscous fluxes. The second-order dual-time stepping method was used for temporal integration [35,36] and the nondimensional time-step size was  $\Delta t = 1.8 \times 10^{-3}$  with respect to the convective time scale  $t_c = c/U_{\infty}$ . The Courant–Friedrichs–Lewy number for the inner iteration was 2.5, with 12 iterations for sufficient inner-iteration convergence. For every iteration, a multigrid technique was used to accelerate solution convergence. An adiabatic wall condition was applied at the airfoil surface, and a periodic condition was adopted in the span direction. Parallel computations, involving 1224 multiblock structures, were performed using the Intel Xeon Phi Knights Landing (KNL) processors of the NURION supercomputing system at the Korea Institute of Science Technology Information.

**Table 2** Computational grids around the external flow (Ext) and actuator (Act) tested in the current study. N indicates the number of grid points and  $\Delta$  indicates the grid length. Subscripts  $\xi$ ,  $\zeta$ , and  $\eta$  indicate the streamwise, wall-normal, and spanwise directions in a generalized coordinate system, respectively, and 1 indicates the first wall adjacent cell.

Grie	d	Nξ	$N_{\zeta}$	$N_{\eta}$	$N_{tot}/10^6$	$\Delta_{\xi,LE}$	$\Delta_{\xi,TE}$	$\Delta_{\zeta,1}^+$	$\Delta_{\eta}$
1	Ext Act	769 129	193 49	193 193	29 1.2	$2 \times 10^{-4}c$	2 × 10 <sup>-4</sup> c	< 1	$5 \times 10^{-3}c$
2	Ext Act	705 113	225 57	121 121	20 0.8	$1\times10^{-4}c$	$2 \times 10^{-4}c$	< 0.25	$8 \times 10^{-3}c$

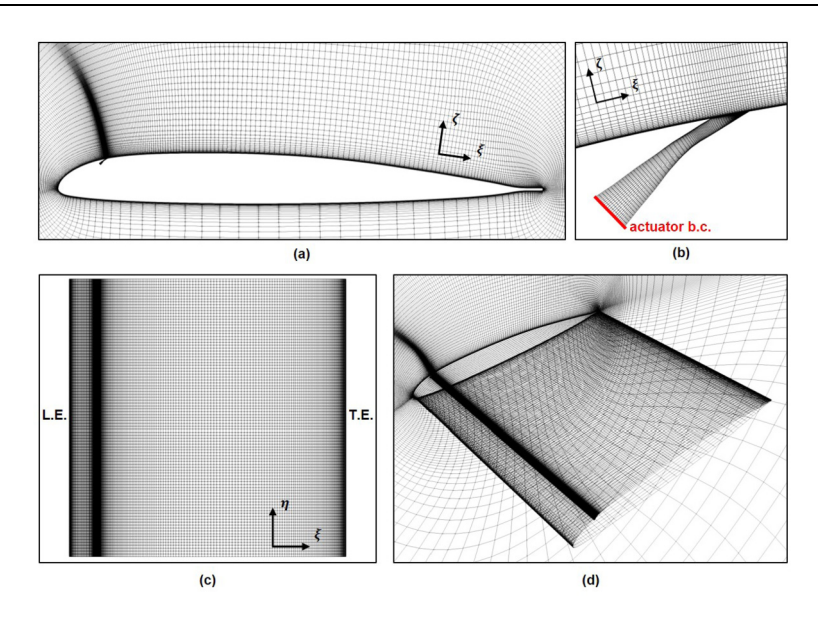


**Fig. 3.** Computational grid generated around VR-12 wing (grid 1 is shown here); (a) cross-sectional view in  $\xi$  and  $\zeta$  coordinates, (b) grid around actuator slot, (c) top view of suction surface in  $\xi$  and  $\eta$  coordinates, and (d) perspective view of the 3-D wing. Every second grid point is shown in all figures.

A delayed detached-eddy simulation based on the Spalart-Allmaras (SA) turbulence model [37–39] was conducted. The transport equation of the standard SA model by Spalart et al. [37] is given as follows:

$$\frac{\partial \tilde{v}}{\partial t} + u_j \frac{\partial \tilde{v}}{\partial x_j} = c_{b1} (1 - f_{t2}) \tilde{S} \tilde{v} - \left[ c_{w1} f_w - \frac{c_{b1}}{\kappa^2} f_{t2} \right] \left( \frac{\tilde{v}}{d} \right)^2 \\
+ \frac{1}{\sigma} \left[ \frac{\partial}{\partial x_j} \left( (\tilde{v} + v) \frac{\partial \tilde{v}}{\partial x_j} \right) + c_{b2} \frac{\partial \tilde{v}}{\partial x_i} \frac{\partial \tilde{v}}{\partial x_i} \right]$$
(1)

and the turbulent viscosity is calculated using  $v_t = \tilde{v} f_{v1}$ , where  $f_{v1} = \chi^3/(\chi^3 + C_{v1}^3)$  and  $\chi = \tilde{v}/v$ . For the eddy-resolving simulation, d in the destruction term of Eqn (1) is set as  $d = d_w - f_d \max(0, d_w - C_{DES}\Delta)$ , where  $f_d$  is the delay function for the DDES model,  $d_w$  is the minimum distance from the field point to the wall,  $C_{DES} = 0.65$  is the DES constant, and  $\Delta$  is the length scale of a modeled turbulence. The delay function  $f_d$  for the DDES model is computed as  $f_d = 1 - \tanh([8r_d]^3)$ , where  $r_d = (v_t + v)/(|\nabla U|\kappa^2 d_w^2)$  and  $\kappa = 0.41$ . In the current study, the length scale  $\Delta$  was computed using the cube-root cell volume  $\Delta = (\Delta \xi \Delta \eta \Delta \zeta)^{1/3}$ . A freestream condition for the SA working variable  $\tilde{v}_\infty = 4v_\infty$ , which is an approach recommended by previous studies [40,41], was applied.

# 2.2. Actuator boundary condition

In the wind tunnel experiments in [23,24], combustion processes inside the COMPACT module impulsively increased pressures and generated high-speed jets toward the external flow. In this computational study, the momentary pressure rise measured in the tests [23,24] was assigned to the bottom of the actuator slot,

instead of modeling the full combustion process inside the chamber. The impulsive pressure variation was modeled as a discretely distributed pulse, as depicted in Fig. 4. Based on measurements from these wind tunnel tests [23,24], a peak pressure ratio of  $p_{r,peak}=2.47$  and a pulse duration of  $t_p=0.18t_c=0.7$  ms were adopted as a standard for this study, and the impacts of their variations were assessed numerically, which will be discussed in the later section.

The boundary conditions at the bottom of the actuator slot (Figs. 2 and 3) are summarized in Eqs. (2) and (3),

$$p_{act} = p_r p_{ref}, \quad T_{act} = p_{act}/(\rho_{\infty} R),$$
 (2)

$$p_{noact} = p_{nb} - \left(\frac{\partial p}{\partial n}\right)_{nb} \Delta n, \quad T_{noact} = T_{nb,tot}, \tag{3}$$

where the subscripts *act* and *noact* denote the actuating and non-actuating periods, *nb* is neighboring cell, respectively.

A characteristic inflow condition was assigned for the pulse duration  $t_p$ . The time-varying actuation pressure  $p_{act}$  was obtained using the pressure ratio  $p_r(t)$  depicted in Fig. 4 using the reference pressure  $p_{ref}$  at the slot bottom immediately before the pulse operation. The actuation temperature  $T_{act}$  was determined based on the ideal gas law using  $p_{act}$ , gas constant R, and freestream density  $\rho_{\infty}$ . The jet velocity was calculated using the Riemann invariant with  $p_{act}$  and  $T_{act}$  at each time step. The actuation condition for the SA variable  $\tilde{\nu}$  is identical to the freestream condition for a stable computation, where  $\tilde{\nu}_{act}/\nu_{\infty}=4$  was assumed for turbulent inflow from the combustion chamber (not resolved here). A zeromass-flux condition was assigned to the non-actuating period. The pressure  $p_{noact}$  was linearly extrapolated from the neighboring cell nb in the boundary-normal direction n, and the temperature  $T_{noact}$ 

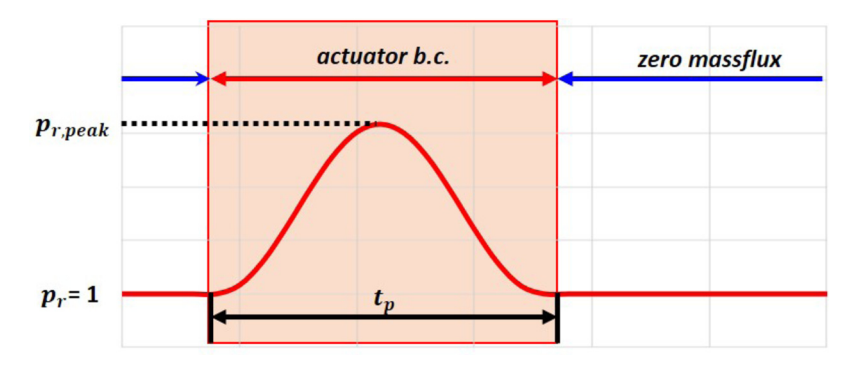


**Fig. 4.** Impulsive variation in pressure with a pulse duration  $t_p$  at the actuator boundary.

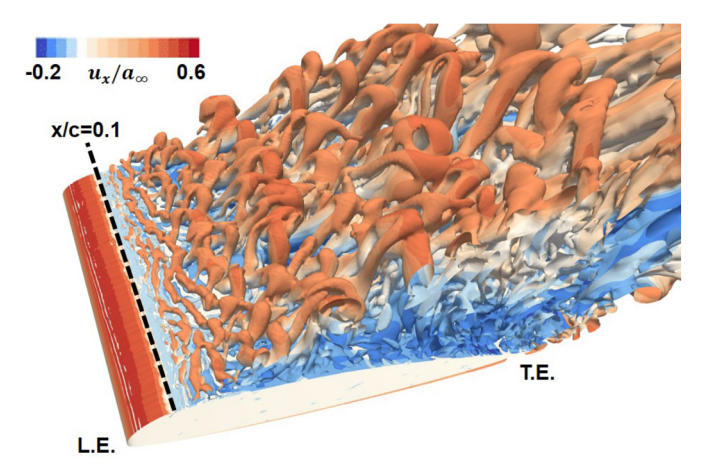


**Fig. 5.** Instantaneous flow structure around the baseline wing at  $Re = 2.6 \times 10^6$ , Ma = 0.3 and  $\alpha = 20^\circ$ , visualized with Q-criterion Q = 1 colored by streamwise velocity  $u_x/a_\infty$ . The actuator location is denoted by dashed line at x/c = 0.1. (For interpretation of the colors in the figure(s), the reader is referred to the web version of this article.)

was set to be the total temperature of the neighboring cell nb based on an isentropic relationship. An adiabatic solid wall was used as the slot sidewall.

# 3. Results and discussion

# 3.1. Baseline flow

The flow structures around the baseline flow, *i.e.*, without actuation, are shown in Fig. 5, which reveals a massive flow separation around the baseline VR-12 wing. The vortical structures shown in Fig. 5 were identified using the Q-criterion and colored with the streamwise velocity  $u_x$ . The flow near the leading edge was well attached to the surface, and separation occurred at approximately  $x/c \simeq 0.1$ , yielding a massive vortical structure. Thus, severe reverse flow was observed on the suction side, which was reminiscent of a stalled wing.

The skin friction coefficient,  $C_f = \tau_w/(0.5\rho_\infty U_\infty^2)$ , around the baseline wing is shown in Fig. 6, which is associated with the massive flow separation shown in Fig. 5. The current computational results shown in Fig. 6 were time-averaged over  $30t_c$  in a quasisteady state after sufficient time  $\Delta t = 20t_c$  from the uniform initial condition. For additional comparison, the URANS result was also plotted. For both DDES cases, a separation bubbles was observed near the leading edge  $(x/c \simeq 0.02)$ , which is also shown in Fig. 5, whereas the URANS approach exhibited a different prediction for the upstream part. The downstream part of the wing exhibited flattened skin friction, which was mainly due to the severely separated flow observed for x/c > 0.1.

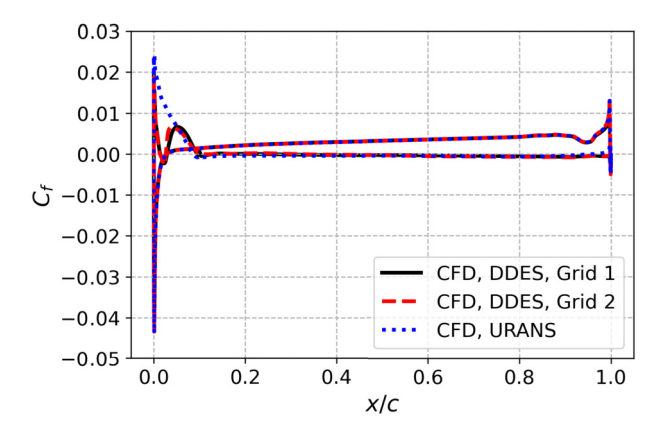


**Fig. 6.** Time- and span-averaged skin friction around baseline VR-12 wing at  $Re=2.6\times10^6$ , Ma=0.3 and  $\alpha=20^\circ$ .

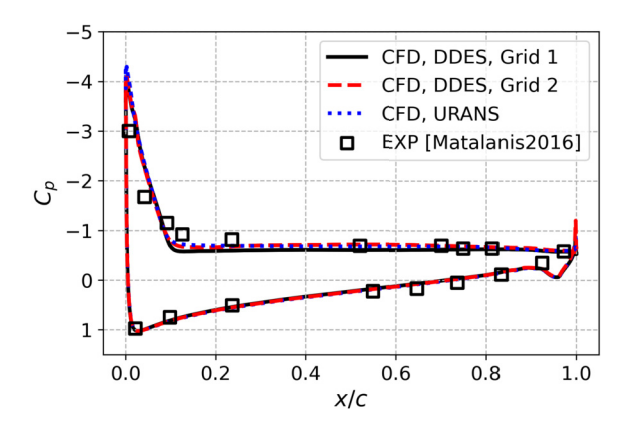


**Fig. 7.** Time- and span-averaged pressure distribution around baseline VR-12 wing at  $Re=2.6\times10^6$ , Ma=0.3 and  $\alpha=20^\circ$ .

The pressure distribution,  $C_p = (p-p_\infty)/(0.5\rho_\infty U_\infty^2)$ , was compared with relevant experimental results, and the current computation showed good agreement with the test data (see Fig. 7). A rapid decrease in the suction pressure near the leading edge  $(x/c \lesssim 0.1)$  was observed with a flattened pressure profile on the overall suction side, which is ascribed to the massively separated flow. Because the flowfield solutions for the two different grids yielded similar results, grid 1 was chosen for the flow calculations in the remaining part of the study, including the cases involving actuation.

Fig. 8 shows the instantaneous turbulent variables at midspan, including the eddy viscosity  $\nu_t$  and the DDES shielding parameter  $f_d$ . In this figure, the shielding parameter at  $f_d=0.5$  is indicated with a red line as the boundary between the RANS and LES regions. The current computation showed a rapid transition from RANS to LES near the wall; therefore, a thin RANS layer was ob-

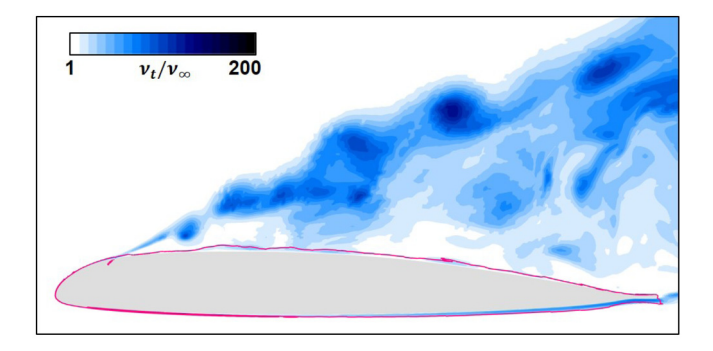
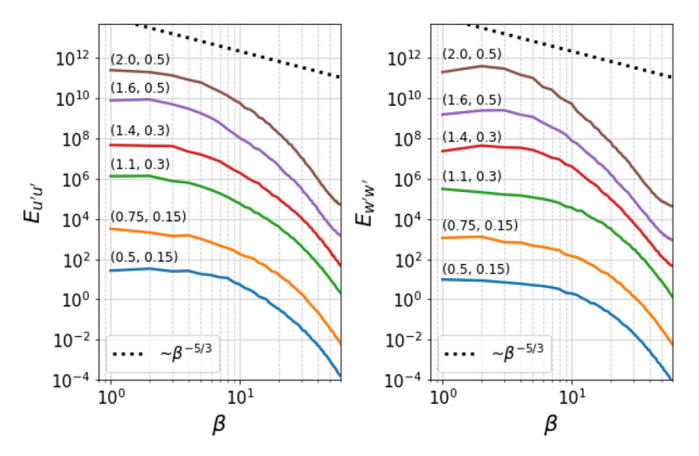


**Fig. 8.** Instantaneous turbulent flowfields in the baseline computation. Eddy viscosity  $\nu_t$  is nondimensionalized with a freestream molecular viscosity  $\nu_{\infty}$ . The boundary between RANS and LES regions is visualized with a red contour line of the DDES shielding parameter at  $f_d = 0.5$ .



(a) Spanwise energy spectrum

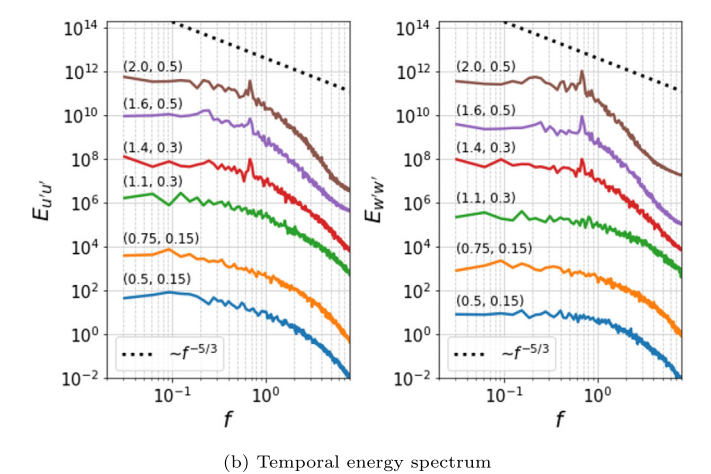


**Fig. 9.** One-dimensional power spectra of the streamwise and wall-normal velocity fluctuations, u' and w', at six selected locations (x/c,z/c) in the LES region. Spanwise wavenumber  $\beta$  and frequency f are nondimensionalized with fundamental wavenumber and freestream convecting frequency  $(1/t_c)$ , respectively. Each spectrum is shifted by two orders of magnitude from (x/c,z/c)=(0.5,0.15).

served around the lifting surface. Here, the large LES region on the suction side could be associated with the minimum eddy viscosity calculated for the wake region, which is favorable to resolving turbulent structures with low numerical dissipation.

The one-dimensional power spectra of the baseline flow were analyzed, as shown in Fig. 9. The power spectrum was obtained using the fast Fourier transformation of the fluctuating velocities at selected locations (x/c, z/c) in the LES region. The time averaging is applied to the spanwise spectrum, and the wavenumber  $\beta$  is

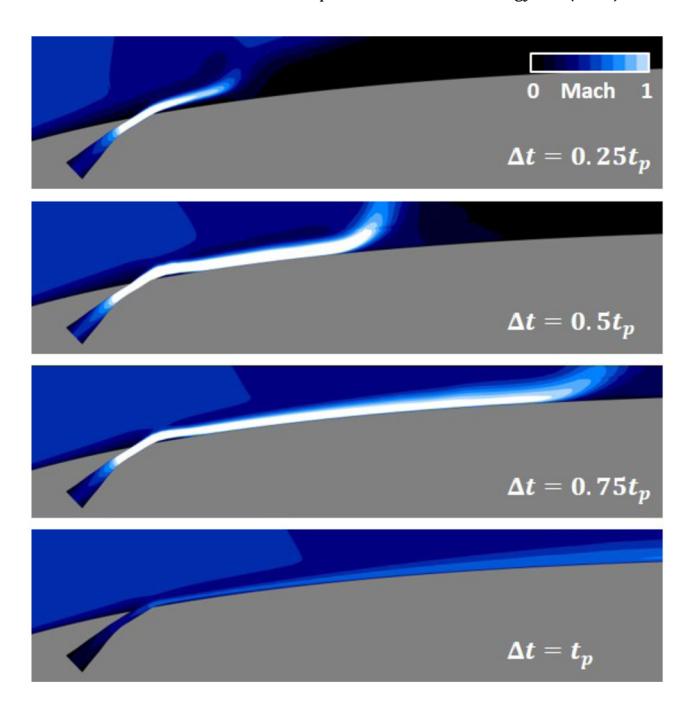


**Fig. 10.** A high speed jet generated from impulsive actuation with a peak pressure ratio  $p_r$ ,  $p_{eak} = 2.47$  and a pulse duration  $t_p = 0.7$  ms  $\simeq 0.18t_c$ . Flowfields are visualized at the midspan location, and the white region indicates that the flow is supersonic, i.e., Ma > 1.

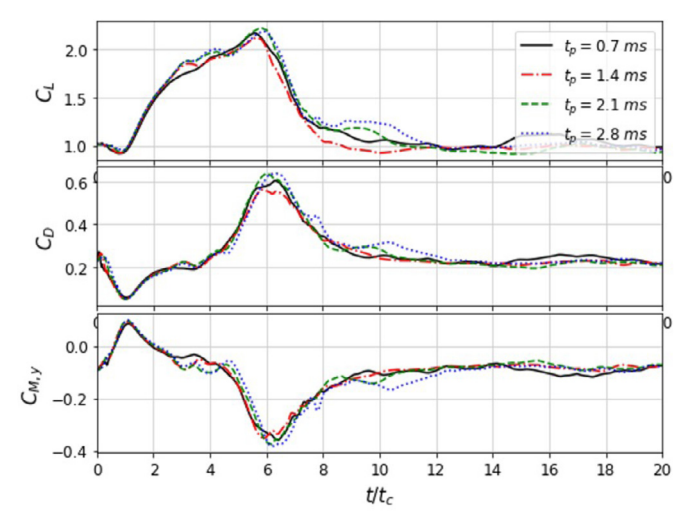
nondimensionalized with the fundamental wavenumber. The spanwise averaging is performed to the temporal spectrum, and the frequency f is nondimensionalized with the freestream convection frequency,  $1/t_c$ . The inertial subrange in the current computation, indicated by the slope -5/3, was well captured in the spanwise and temporal domains. The spanwise spectrum agrees well with the wavenumber range up to  $\beta \simeq 30$ , which implies that the grid strategy can capture a wave that is approximately six times the spanwise grid size or larger. A similar energy decline is observed in the temporal spectrum accompanied by a local peak amplitude around  $f \simeq 0.7$ . It is probably related to a vortex shedding in the wake region, which is also observed in relevant measurements [42,43].

# 3.2. Controlled flow

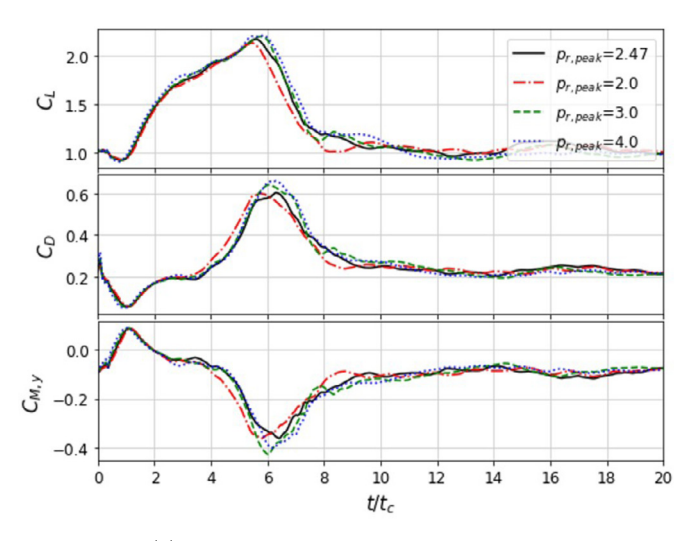
# 3.2.1. Jet application and transient dynamics of forces and moment

Fig. 10 illustrates the jet flow generated via impulsive actuation with a peak pressure ratio of  $p_{r,peak} = 2.47$  and pulse duration of  $t_p = 0.7$  ms  $\simeq 0.18t_c$ , which were identical to the experimental conditions [23,24]. At  $\Delta t = 0.25t_p$ , the flow in the actuator slot was choked at the nozzle throat, and thus a supersonic jet (the white region in Fig. 10) was generated and merged into the external flow. From  $\Delta t = 0.5t_p$  to  $\Delta t = 0.75t_p$ , the jet flow covered the downstream of the actuator location. After  $\Delta t = t_p$ , the highmomentum jet vanished because of the termination of the pulse. The peak jet-momentum coefficient  $C_{\mu} = (\rho U^2 h)_{jet}/(\rho U^2 c)_{\infty}$  was calculated based on the normal component of the velocity to be at the throat of the nozzle, and exhibited a value of  $C_{\mu,peak} \simeq$  $2 \times 10^{-2}$ , which is comparable to the experimental value  $C_{\mu,peak} =$  $1.9 \times 10^{-2}$  reported in [23,24]. It is thus inferred that the current computational approach can reproduce the jet flow tested in the experiments [23,24] with a comparable jet momentum.

The transient responses of the aerodynamic forces and moment with respect to the impulsive actuation are shown in Fig. 11. As discussed in Section 2, a pulse duration of  $t_p = 0.7$  ms and  $p_{r,peak} = 2.47$  were applied as a standard based on experimen-



(a) Variations in pulse duration  $t_n$ 



(b) Variations in peak pressure ratio  $p_{r,peak}$ 

**Fig. 11.** Transient dynamics in the aerodynamic lift  $C_L = \frac{1}{0.5\rho_{\infty}U_{\infty}^2A}$ , drag  $C_D = \frac{D}{0.5\rho_{\infty}U_{\infty}^2A}$  and moment  $C_{M,y} = \frac{M}{0.5\rho_{\infty}U_{\infty}^2Ac}$  from impulsive actuation with variations in a pulse duration  $t_p$  (a) and peak pressure ratio  $p_{r,peak}$  (b). Jet flow is applied to the baseline wing at  $\Delta t = 0$ . Note that  $t_p = 0.7$  ms and  $p_{r,peak} = 2.47$  were based on measurements in [23,24].

tal measurements from previous studies [23,24], and the impact of the actuation parameters on the force hysteresis was assessed. The pulse durations that were tested ranged from  $t_p$  =0.7 to 2.8 ms (see Fig. 11a), and the peak pressure ratio was varied from  $p_{r,peak}$  =2 to 4 (see Fig. 11b).

The computational results shown in Fig. 11 imply that the parameter variation yielded minimum differences in the forces and moment hysteresis, at least in the ranges tested in the current study. In all cases tested, it was observed that the aerodynamic forces and moment changed rapidly in the early stages and gradually returned to the baseline flow in the later stages. As impulsive actuation was applied to the baseline at  $\Delta t = 0$ , the aerodynamic lift quickly varied in the early stages after the actuation. The lift force was significantly enhanced for  $\Delta t/t_c \simeq 2$  with minimum changes in drag and moment. After  $\Delta t/t_c \gtrsim 3$ , the lift forces exhibited a peak value of  $C_L \simeq 2.2$  at  $\Delta t/t_c \simeq 5.5$ , accompanied by additional drag and moment amplitude. After a severe lift drop, in conjunction with the peak drag and moment amplitude, at  $\Delta t/t_c \simeq 6$ , the forces and moment returned to the baseline after  $\Delta t/t_c > 10$ .

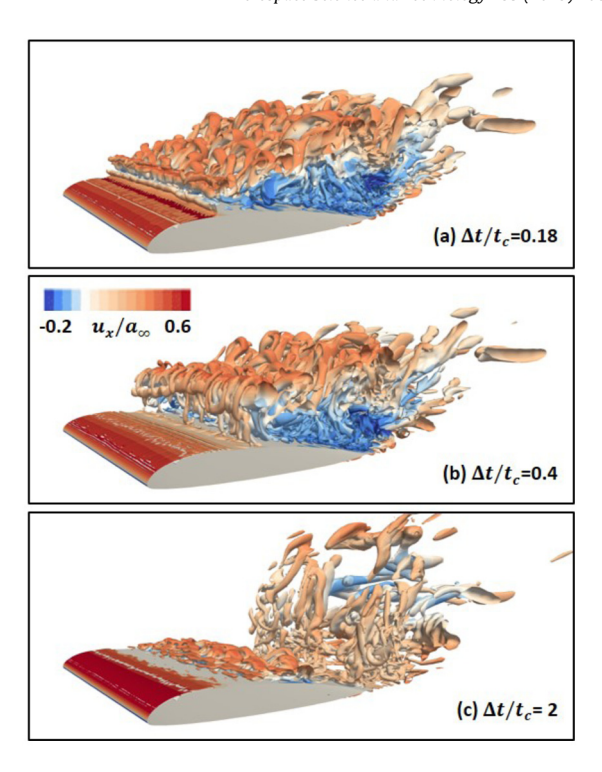


**Fig. 12.** Flow structures around the actuated VR-12 wing at three selected times in the reattachment stages ( $0 \le \Delta t/t_c \lesssim 3$ ).

In the next part of the study, presented in Sections 3.2.2 and 3.2.3, detailed flow physics associated with the force variations will be investigated for two time windows. Section 3.2.2 will focus on the early stages, where the flow is quickly reattached via jet actuation ( $0 \le \Delta t/t_c \lesssim 3$ , reattachment stages). Section 3.2.3 will discuss the later stages, in which recirculating flow on the suction side dominates gradual variations in the aerodynamic forces and moment ( $\Delta t/t_c \gtrsim 3$ , recirculation stages). Because the actuation parameters yielded minimum variations in the overall force hysteresis (see Fig. 11), a detailed investigation based on the standard values,  $t_p = 0.7$  ms and  $p_{r,peak} = 2.47$  will be presented in later sections of this paper.

# 3.2.2. Reattachment stages

A quick reattachment of the external flow with the jet actuation and corresponding vortical structures around the actuated VR-12 wing are illustrated in Fig. 12. The phenomenon shown induced a rapid increase in the lift force after the jet initiation ( $\Delta t=0$ ), as shown in Fig. 11. At  $\Delta t/t_c=t_p/t_c=0.18$ , the flow near the actuator strongly interacted with the jet flow, and a reattached flow was observed (see Fig. 12). At  $\Delta t/t_c=0.4$ , the reattached region became wider than in the previous timing, accompanied by a suppression of the wake flow. After  $\Delta t/t_c=2$ , the wake flow vanished from the surface, while the reattached region remained on the suction side, especially near the leading edge.

The skin friction  $C_f$  distribution around the wing, which is associated with the quick reattachment process that occurs with jet actuation, is depicted in Fig. 13. At the early stage,  $\Delta t/t_c=0.18$ , a high amplitude of  $C_f$  was observed downstream of the actuator, which could be due to the jet actuation. After  $\Delta t/t_c=0.4$ , the reattached region then became wider than the previous timing. From  $\Delta t/t_c=1$  to 3, the flow near the leading edge  $(x/c\leq0.2)$  was strongly attached to the surface. Thus, the skin friction  $C_f$  near the leading edge constantly increased, which could yield significant improvements in the lift force at the corresponding time window. At the same time, a locally recirculating flow was observed around the midchord.

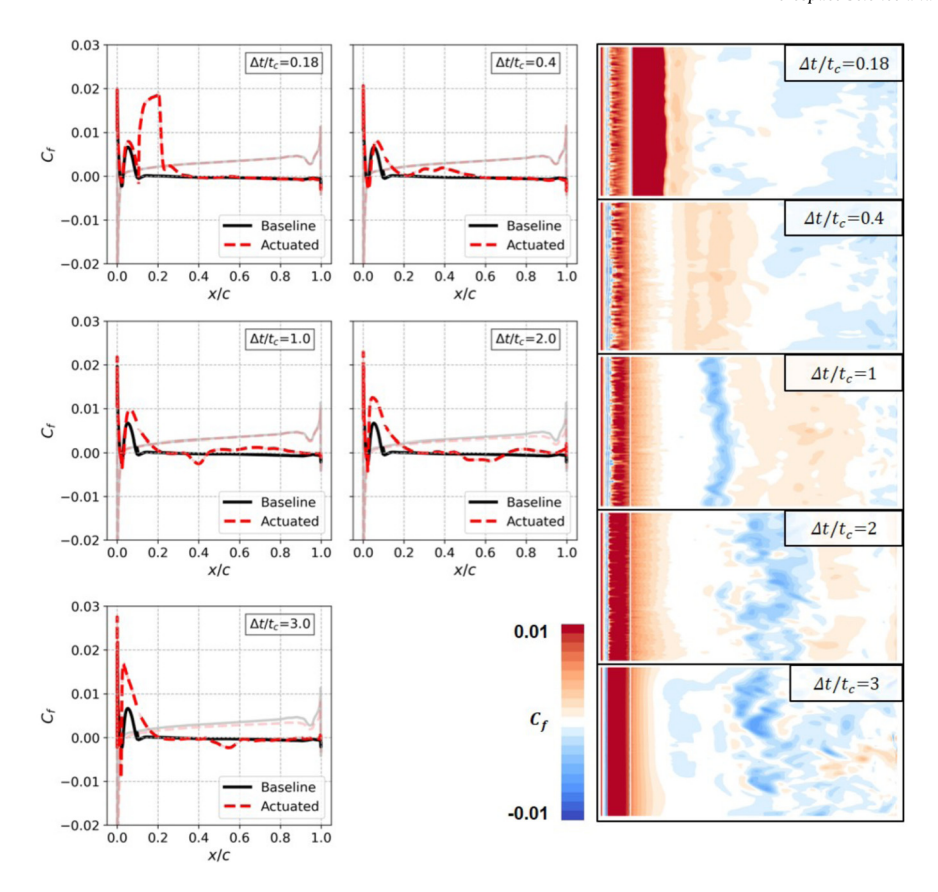


Fig. 13. Span-averaged  $C_f$  profiles highlighted on the suction side (left) and top views of  $C_f$  distribution with a half scaled span (right) at five selected times during the reattachment stages ( $0 \le \Delta t/t_c \lesssim 3$ ).

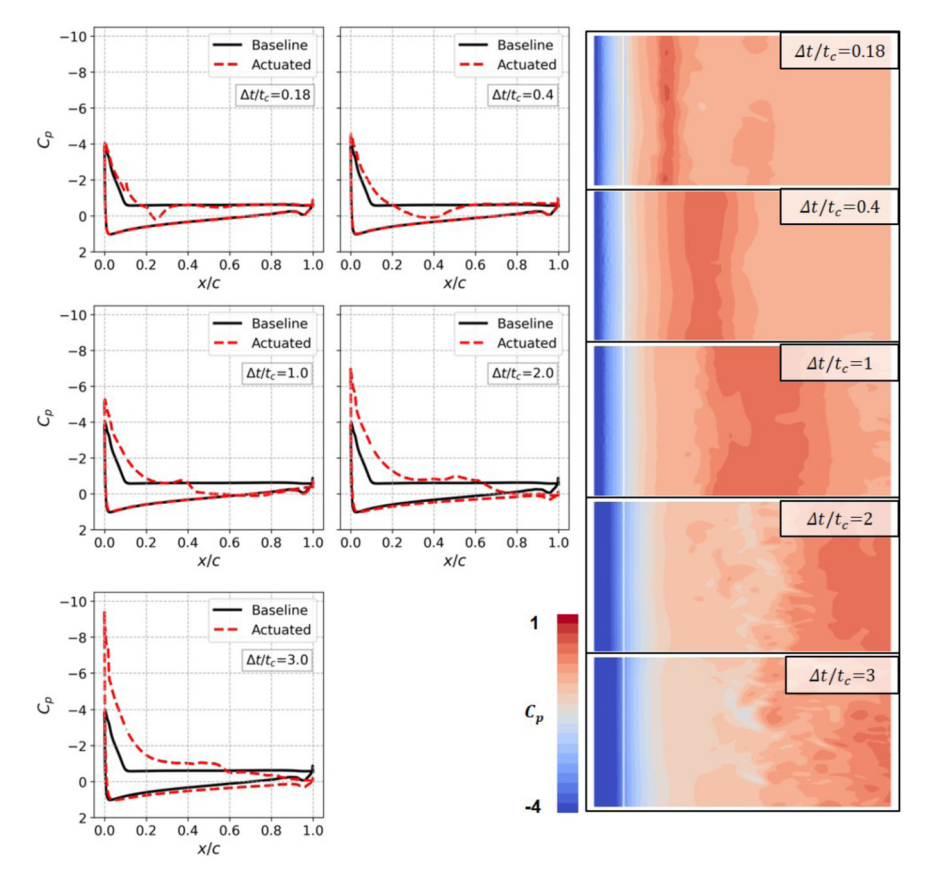


Fig. 14. Span-averaged  $C_p$  profiles highlighted on the suction side (left) and top views of  $C_p$  distribution with a half scaled span (right) at five selected times during the reattachment stages ( $0 \le \Delta t/t_c \lesssim 3$ ).

Fig. 14 shows the pressure distribution around the actuated wing, which was closely related to the forces and moment dynamics shown in Fig. 11. From  $\Delta t/t_c=0.18$  to 0.4, the pressure loop around the wing was changed mainly by the jet interaction. The suction peak constantly increased from  $\Delta t/t_c=1$  to 3, which could be related to the strongly attached flow for  $x/c\lesssim0.2$  (see Fig. 13). The high-pressure region due to the jet interaction faded away from the trailing edge after  $\Delta t/t_c\geq2$ . Although a locally recirculating flow was observed around the midchord, as shown in Fig. 13, it yielded minimum impact on the pressure distribution shown in Fig. 14.

The present chapter describes the quick reattachment process in the early stages of transient dynamics with the actuation. A jet flow is generated from the impulsive actuation with a pulse duration of  $\mathcal{O}(0.1t_c)$  and strongly interacts with the external flow on the suction side. It is noted that the high-speed jet reattaches the flow and promotes an increase in the suction peak near the leading edge, which can enhance the lift force for  $\mathcal{O}(t_c)$ .

# 3.2.3. Recirculation stages

Flow structures in the recirculation stages are visualized in Fig. 15, which shows a gradual recovery to the baseline flow. At  $\Delta t/t_c=4$ , a reverse-flow region around the midchord became more energetic than to the previous time window in the reattachment stages (see Section 3.2.2). A spanwise variation in the flow reversal is observed despite the uniform numerical setups to the jet actuation, which could be due to the three-dimensionality of flow near the leading edge (see Fig. 5). From  $\Delta t/t_c=6$  to 7.5, the reverse flow covered the whole suction side from the upstream, and was detached from the wing surface. It could result in the nominal lift drop and the peak drag and moment at the corresponding timing shown in Fig. 11. After the detachment process, the flow completely returned to the baseline (see  $\Delta t/t_c=14$ ), and thus the flow field exhibited a structure similar to that of the baseline flow shown in Fig. 5.

The skin friction  $C_f$  around the wing, shown in Fig. 16, is associated with the flow dynamics that occur with the recirculation shown in Fig. 15. At  $\Delta t/t_c=4$ , the recirculating flow around the midchord became stronger than in the reattachment stages, and thus a negative  $C_f$  was clearly observed at approximately  $x/c\simeq 0.5$ . At  $\Delta t/t_c=6$ , the  $C_f$  amplitude near the leading edge rapidly decreased, and a strong reverse flow was observed for  $x/c\geq 0.4$ , which probably resulted in the lift drop and the peak drag and moment (see  $\Delta t/t_c=6$  in Fig. 11). Finally, the impact of the jet actuation on the flow behavior was reduced ( $\Delta t/t_c=6$  to 8), and the skin friction on the suction side finally returned to the baseline ( $\Delta t/t_c=14$ ).

The pressure distribution  $C_p$  around the wing, shown in Fig. 17, is relevant to the gradual variations in forces and moment. At  $\Delta t/t_c=4$ , a low pressure around the midchord due to the recirculating flow was observed, and generated additional lift force, drag, and moment amplitude at  $\Delta t/t_c \gtrsim 4$  (see Fig. 11). From  $\Delta t/t_c=4$  to 7, the suction peak near the leading edge was reduced to the baseline, accompanied by a wide low-pressure region on the suction side, which could yield a lift drop and the peak drag and moment (see Fig. 11). After  $\Delta t/t_c \geq 8$ , the flow control impact on the flow feature was constantly reduced, and thus the pressure distribution around the wing recovered to the baseline and yielded results similar to those of the baseline case ( $\Delta t/t_c=14$ ).

In the present section, the transient flow features that are associated with the gradual changes in the forces and moment in the later stages after jet initiation are explained. The variations in aerodynamic force and moment in the reattachment stages were mainly due to a low-pressure region on the suction side from recirculation. This low-pressure region increases more largely on the suction surface and drives the generation of additional lift, which

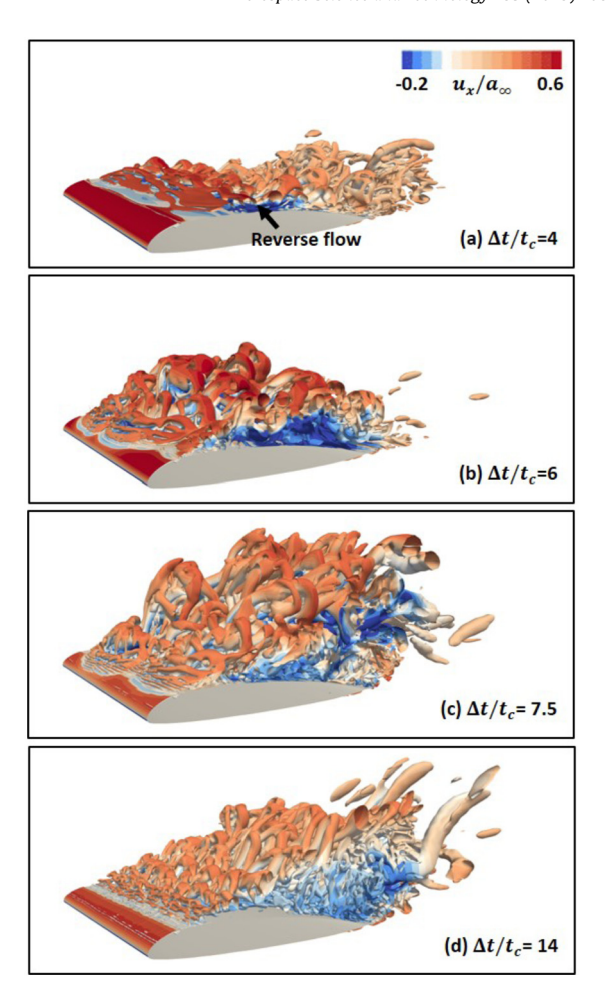


**Fig. 15.** Flow structures around the actuated VR-12 wing at four selected times in the recirculating stages ( $\Delta t/t_c \gtrsim 3$ ).

is accompanied by a drag and moment increment. As the high suction peak (obtained in the reattachment stages) decreases to the baseline, the impact of the jet actuation diminishes. Finally, the flow recovers to the baseline after approximately  $O(10t_c)$  from the jet initiation.

# 4. Conclusions

A separated flow around a lifting body was transiently controlled via a high-speed jet actuation, and flow features associated with the transient dynamics were numerically investigated. Impulsive jet actuation was applied to a separated flow around a stalled VR-12 wing, using a modeled actuator boundary condition representing a COMPACT module in experiments.

The high-speed jet was generated through a choked flow at a nozzle and strongly interacted with the external flow. Interactions between the jet and external flow dynamically changed flow characteristics around the wing and yielded long transient variations in the forces and moment after the actuation. The force hysteresis revealed that the aerodynamic forces and moment rapidly varied in the early stages after jet initiation, and that the flow control impact diminished gradually over a time scale in an order of magnitude longer than the freestream convection.

Detailed investigations on the flow characteristics with respect to the actuation were pursued, and numerical results revealed two distinct features associated with the transient dynamics: reattachment and recirculation. A quick reattachment process in the early stages after the jet initiation generated a high suction peak near

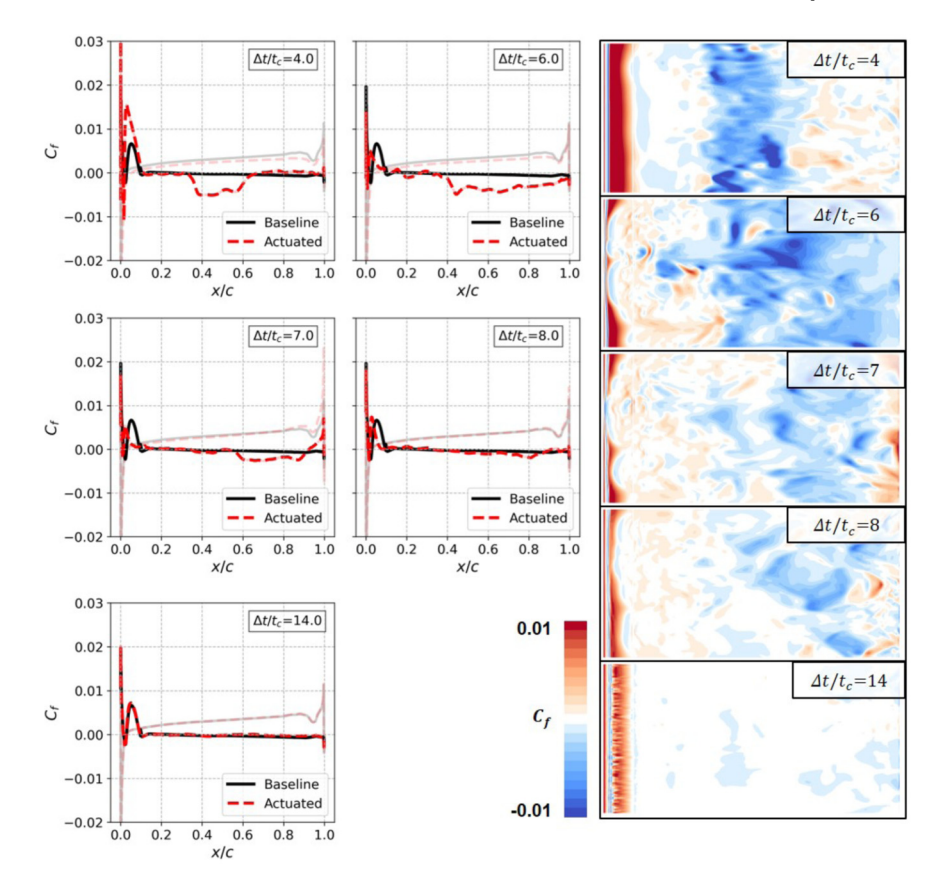


**Fig. 16.** Span-averaged  $C_f$  profiles highlighted on the suction side (left) and top views of  $C_f$  distribution with a half scaled span (right) at five selected times during the recirculation stages  $(\Delta t/t_c \gtrsim 3)$ .

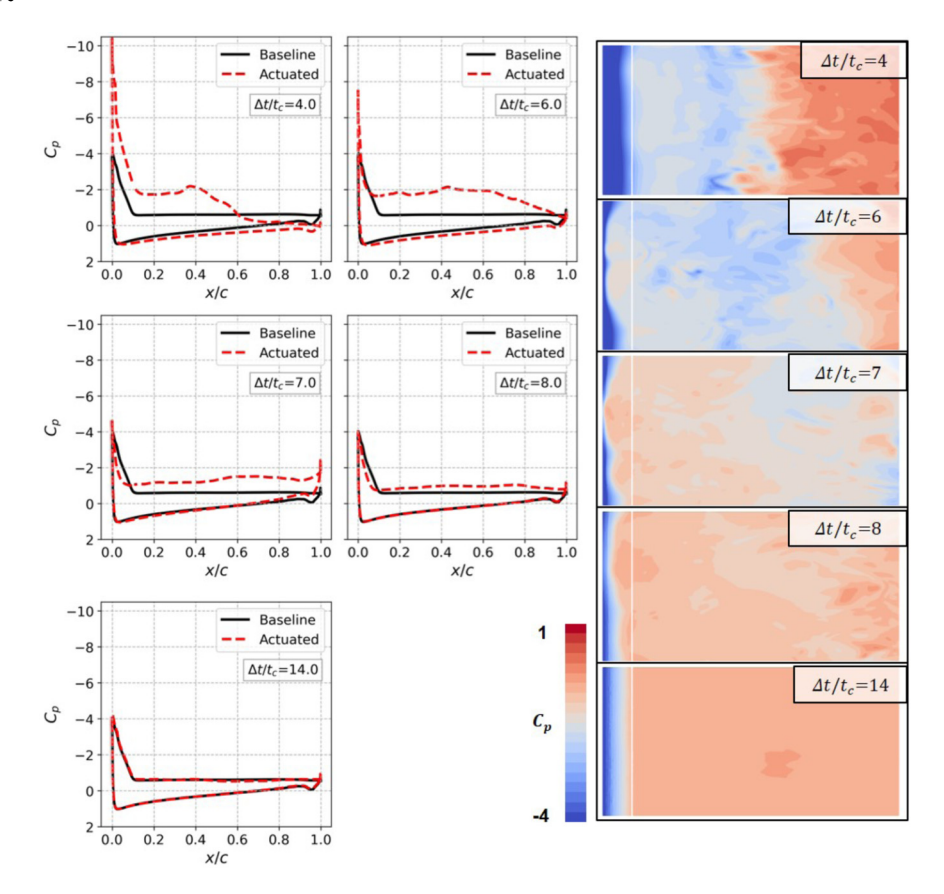


Fig. 17. Span-averaged  $C_p$  profiles highlighted on the suction side (left) and top views of  $C_p$  distribution with a half scaled span (right) at five selected times during the recirculation stages  $(\Delta t/t_c \gtrsim 3)$ .

the leading edge compared to that of the baseline case, which improved the lift force rapidly. Subsequently, the recirculating flow was observed in the later stages after the actuation and induced a low-pressure region, which generated additional lift accompanied by a drag and moment increment. The flow control impact diminished by the high suction peak near the leading edge decreased to the baseline, and the flow around the wing finally returned to the baseline.

# **Declaration of competing interest**

The authors declare that they have no known competing financial interests or personal relationships that could have appeared to influence the work reported in this paper.

# Data availability

Data will be made available on request.

# **Acknowledgements**

This work was supported by the Korea Institute of Science and Technology Information (KISTI) institutional R&D Program (K-22-L02-C05-S01 and K-22-L05-C02-S07) with the NURION supercomputing resources, including technical support (TS-2021-RE-0023 and TS-2022-RE-0008).

# Appendix A. Supplementary material

Supplementary material related to this article can be found online at https://doi.org/10.1016/j.ast.2023.108171.

# References

- [1] M. Gad-el-Hak, Flow Control Passive, Active, and Reactive Flow Management, Cambridge University Press, 2007.
- [2] P.R. Ashill, J.L. Fulker, K.C. Hackett, A review of recent developments in flow control, Aeronaut. J. 109 (1095) (2005) 205–232, https://doi.org/10.1017/ S0001924000005200.
- [3] L.N. Cattafesta, M. Sheplak, Actuators for active flow control, Annu. Rev. Fluid Mech. 43 (1) (2011) 247–272, https://doi.org/10.1146/annurev-fluid-122109-160634.
- [4] K.W. Mcalister, C. Tung, Suppression of dynamic stall with a leading-edge slat on a VR-7 airfoil, Tech. Rep. NASA-TP-3357, NASA, 1993.
- [5] A. Mishra, J.D. Baeder, D.G. Opoku, B.E. Wake, R.-S. Lin, Coupled CFD/CSD prediction of the effects of leading edge slat on rotor performance, in: 65th Annual Forum and Technology Display of the American Helicopter Society International, Dallas, TX, USA, 2009.
- [6] P.F. Lorber, A. Bagai, B.E. Wake, Design and evaluation of slatted airfoils for improved rotor performance, in: 62nd Annual Forum and Technology Display of the American Helicopter Society International, Phoenix, AZ, USA, 2006.
- [7] M.P. Kinzel, M.D. Maughmer, G.A. Lesieutre, Miniature trailing-edge effectors for rotorcraft performance enhancement, J. Am. Helicopter Soc. 52 (2) (2007) 146–158, https://doi.org/10.4050/JAHS.52.146.
- [8] C.G. Matalanis, B.E. Wake, D. Opoku, B.-Y. Min, N. Yeshala, L. Sankar, Aerodynamic evaluation of miniature trailing-edge effectors for active rotor control, J. Aircr. 48 (3) (2011) 995–1004, https://doi.org/10.2514/1.c031191.
- [9] M.L. Post, T.C. Corke, Separation control using plasma actuators: dynamic stall vortex control on oscillating airfoil, AIAA J. 44 (12) (2006) 3125–3135, https:// doi.org/10.2514/1.22716.
- [10] A. Darabi, I. Wygnanski, Active management of naturally separated flow over a solid surface. Part 1. The forced reattachment process, J. Fluid Mech. 510 (2004) 105–129, https://doi.org/10.1017/S0022112004009231.
- [11] A. Darabi, I. Wygnanski, Active management of naturally separated flow over a solid surface. Part 2. The separation process, J. Fluid Mech. 510 (2004) 131–144, https://doi.org/10.1017/S0022112004009243.
- [12] A. Rehman, K. Kontis, Synthetic jet control effectiveness on stationary and pitching airfoils, J. Aircr. 43 (6) (2006) 1782–1789, https://doi.org/10.2514/1. 20333.
- [13] K. Taylor, M. Amitay, Dynamic stall process on a finite span model and its control via synthetic jet actuators, Phys. Fluids 27 (7) (2015) 077104, https:// doi.org/10.1063/1.4927586.

- [14] H.F. Müller-Vahl, C. Strangfeld, C.N. Nayeri, C.O. Paschereit, D. Greenblatt, Control of thick airfoil, deep dynamic stall using steady blowing, AIAA J. 53 (2) (2015) 277–295, https://doi.org/10.2514/1.J053090.
- [15] J. Deparday, K. Mulleners, Modeling the interplay between the shear layer and leading edge suction during dynamic stall, Phys. Fluids 31 (10) (2019) 107104, https://doi.org/10.1063/1.5121312.
- [16] S. Santra, D. Greenblatt, Dynamic stall control model for pitching airfoils with slot blowing, AIAA J. 59 (1) (2021) 400–404, https://doi.org/10.2514/1.j059818.
- [17] T. Crittenden, A. Glezer, R. Funk, D. Parekh, Combustion-driven jet actuators for flow control, in: 15th AIAA Computational Fluid Dynamics Conference, Anaheim, CA, USA, 2001, AIAA-2001-2768.
- [18] T.M. Crittenden, G.T.K. Woo, A. Glezer, Combustion-powered actuation for transitory flow control, AIAA J. 56 (9) (2018) 3414–3435, https://doi.org/10.2514/1. i056783
- [19] D.P. Brzozowski, G.T.K. Woo, J.R. Culp, A. Glezer, Transient separation control using pulse-combustion actuation, AIAA J. 48 (11) (2010) 2482–2490, https:// doi.org/10.2514/1.45904.
- [20] G.T.K. Woo, A. Glezer, Controlled transitory stall on a pitching airfoil using pulsed actuation, Exp. Fluids 54 (2013) 1507, https://doi.org/10.1007/s00348-013-1507-5.
- [21] G.T.K. Woo, A. Glezer, S. Yorish, T.M. Crittenden, Pulsed actuation control of flow separation on a ROBIN rotorcraft fuselage, AIAA J. 54 (10) (2016) 3274–3289, https://doi.org/10.2514/1.j054008.
- [22] C.G. Matalanis, B.-Y. Min, P.O. Bowles, S. Jee, B.E. Wake, T.M. Crittenden, G. Woo, A. Glezer, Combustion-powered actuation for dynamic-stall suppression: high-Mach simulations and low-Mach experiments, AIAA J. 53 (8) (2015) 2151–2163, https://doi.org/10.2514/1.J055700.
- [23] C.G. Matalanis, P.O. Bowles, S. Jee, B.-Y. Min, A.E. Kuczek, P.F. Croteau, B.E. Wake, T. Crittenden, A. Glezer, P.F. Lorber, Dynamic stall suppression using combustion-powered actuation (COMPACT), Tech. Rep. NASA/CR-2016-219336, NASA Langley Research Center, Hampton, VA, United States, 2016.
- [24] C.G. Matalanis, P.O. Bowles, B.-Y. Min, S. Jee, A.E. Kuczek, B.E. Wake, P.F. Lorber, T.M. Crittenden, A. Glezer, N.W. Schaeffler, High-speed experiments on combustion-powered actuation for dynamic stall suppression, AIAA J. (2017) 3001–3015, https://doi.org/10.2514/1.J055700.
- [25] Y. Tan, T.M. Crittenden, A. Glezer, Aerodynamic control of a dynamically pitching airfoil using pulsed actuation, AIAA J. 60 (6) (2022) 3682–3694, https:// doi.org/10.2514/1.J060722.
- [26] S. Jee, P.O. Bowles, C.G. Matalanis, B.-Y. Min, B.E. Wake, T. Crittenden, A. Glezer, Computations of combustion-powered actuation for dynamic stall suppression, in: AHS 72nd Annual Forum, West Palm Beach, Florida, USA, 2016.
- [27] T. Kim, J. Kim, S. Kim, J. Lee, S. Jee, Unsteady impulsive jet applied to a stalled airfoil, in: Tenth International Conference on Computational Fluid Dynamics (ICCFD10), Barcelona, Spain, 2018.
- [28] T. Kim, J. Kim, M. Kim, J. Lee, S. Jee, Dynamic stall control with impulsive jet, in: AIAA Aviation 2019 Forum, 2019, AIAA–3587, https://arc.aiaa.org/doi/abs/ 10.2514/6.2019-3587.
- [29] T. Kim, S. Jee, Numerical investigation of impulsively generated high-speed jet for dynamic stall suppression, Comput. Fluids 251 (2023) 105757, https://doi. org/10.1016/j.compfluid.2022.105757, https://www.sciencedirect.com/science/ article/pii/S0045793022003498.
- [30] T. Kim, S. Kim, J. Lim, J. Kim, S. Jee, Computational study of Mach number effects on dynamic stall, in: Proceedings of the ASME-JSME-KSME 2019 8th Joint Fluids Engineering Conference, vol. 59025, 2019, V001T01A014.
- [31] T. Kim, S. Kim, J. Lim, S. Jee, Numerical investigation of compressibility effect on dynamic stall, Aerosp. Sci. Technol. 105 (2020) 105918, https://doi.org/10. 1016/i.ast.2020.105918.
- [32] P.R. Spalart, C. Streett, Young-person's guide to detached-eddy simulation grids, Tech. Rep. NASA/CR-2001-211032, NASA, 2001.
- [33] S.L. Krist, R.T. Biedron, C.L. Rumsey, CFL3D user's manual (version 5.0), Tech. Rep. NASA/TM-1998-208444, NASA, 1998.
- [34] P.L. Roe, Approximate Riemann solvers, parameter vectors, and difference schemes, J. Comput. Phys. 43 (2) (1981) 357–372, https://doi.org/10.1016/0021-9991(81)90128-5.
- [35] W.K. Anderson, Implicit multigrid algorithms for the three-dimensional flux split Euler equations, Ph.D. thesis, Mississippi State University. Department of Aerospace Engineering, 1986.
- [36] W.K. Anderson, J.L. Thomas, D.L. Whitfield, Multigrid acceleration of the flux-split Euler equations, AIAA J. 26 (6) (1988) 649–654, https://doi.org/10.2514/3. 9940
- [37] P.R. Spalart, S.R. Allmaras, A one-equation turbulence model for aerodynamic flows, in: 30th Aerospace Sciences Meeting and Exhibit, American Institute of Aeronautics and Astronautics, Reno, NV, USA, 1992, AIAA-1992-439.
- [38] P.R. Spalart, W.-H. Jou, M. Strelets, S.R. Allmaras, Comments on the feasibility of LES for wings, and on a hybrid RANS/LES approach, in: Advances in DNS/LES: Direct Numerical Simulation and Large Eddy Simulation, Air Force, Office of Scientific Research, United States, Greyden Press, ISBN 1570743657, 1997, pp. 137–148.
- [39] P.R. Spalart, S. Deck, M.L. Shur, K.D. Squires, M.K. Strelets, A. Travin, A new version of detached-eddy simulation, resistant to ambiguous grid densities, Theor.

- Comput. Fluid Dyn. 20 (2006) 181–195, https://doi.org/10.1007/s00162-006-0015-0
- [40] C.L. Rumsey, Apparent transition behavior of widely-used turbulence models, Int. J. Heat Fluid Flow 28 (6) (2007) 1460–1471, https://doi.org/10.1016/j.ijheatfluidflow.2007.04.003.
- [41] P.R. Spalart, C.L. Rumsey, Effective inflow conditions for turbulence models in aerodynamic calculations, AIAA J. 45 (10) (2007) 2544–2553, https://doi.org/10. 2514/1.29373.
- [42] S. Yarusevych, P.E. Sullivan, J.G. Kawall, On vortex shedding from an airfoil in low-Reynolds-number flows, J. Fluid Mech. 632 (2009) 245–271, https:// doi.org/10.1017/S0022112009007058.
- [43] S. Yarusevych, M.S.H. Boutilier, Vortex shedding of an airfoil at low Reynolds numbers, AIAA J. 49 (10) (2011) 2221–2227, https://doi.org/10.2514/1.J051028.